

Initial ionospheric observations made by the new Resolute incoherent scatter radar and comparison to solar wind IMF

Hasan Bahcivan,¹ Roland Tsunoda,¹ Michael Nicolls,¹ and Craig Heinselman¹

Received 16 April 2010; revised 27 May 2010; accepted 2 June 2010; published 13 August 2010.

[1] The first Resolute incoherent scatter radar observations of the polar ionospheric F region show the fine control of the ionospheric plasma density and flow (electric field) by the solar wind interplanetary magnetic field (IMF). A summary of 8 days of observations is presented and 10 IMF B_z southward turning events during this period are analyzed in terms of the time delay of plasma density enhancements and ionospheric convection intensification with respect to the timing of B_z southward turning. We find that N_e enhancements are strongly tied to strong (≥ 5 nT) IMF B_z southward turnings; arrive 25–75 mins (depending on MLT) after the IMF pulse arrives at the bowshock nose; last as long as B_z stays southward; contain as small as ~ 25 km horizontal substructures; are altitudinally smooth, a characteristic of a solar produced plasma. The most predictable response of ionospheric convection is anti-sunward flow intensification on average ~ 25 mins after B_z southward change. **Citation:** Bahcivan, H., R. Tsunoda, M. Nicolls, and C. Heinselman (2010), Initial ionospheric observations made by the new Resolute incoherent scatter radar and comparison to solar wind IMF, *Geophys. Res. Lett.*, 37, L15103, doi:10.1029/2010GL043632.

1. Introduction

[2] SRI International through a cooperative agreement with the National Science Foundation has recently (in 2009) completed the construction of the northward-looking face of the Resolute incoherent scatter radar (RISR-N) in Resolute Bay, Canada. The new instrument can provide, for the first time, horizontal and altitudinal profiles of electron density to kilometeric resolution, revealing the fine structure of polar plasma density irregularities (patches) as they drift across the electronically steered radar beams. Moreover, line-of-sight ion drift measurements at each beam position enable an analysis of the spatio-temporal variations. Most importantly, spacecraft measurements of solar wind parameters can be compared to RISR ionospheric measurements for prolonged durations to elucidate the detailed response of polar cap convection to solar magnetic field disturbances.

[3] In this letter we present the initial measurements for an 8-day period near equinox in the context of solar wind IMF parameters. First, we provide the RISR parameters and the methods used in extracting the electron density and ionospheric flow. Second, we compare the ionospheric measure-

ments to solar wind parameters measured by the WIND spacecraft. We then select a set of B_z southward turning events and determine the time delays for N_e enhancements and flow intensifications. Finally, an individual plasma density enhancement lasting an hour is further resolved spatially and temporally.

2. Experiment Description

[4] Table 1 shows the system parameters of RISR for this experiment. A total of 11 radar beams were used with the az/el coverage shown in Figure 1. Electron density profiles are obtained by averaging individual beam N_e measurements binned in altitude. The N_e measurements have been calibrated using independent N_e measurements using the plasma line technique. Mean ion drifts were obtained by least-squares fitting a uniform horizontal flow velocity vector to the observed line-of-sight velocities measured between the altitudes of 200–400 km.

3. Observations

[5] Figure 2 shows the N_e altitude profile (averaged over all beam directions) as a function of UT day in September 2009. Superimposed on the color plot is the total electron content in TEC units ($1 \text{ TEC} = 10^{16} \text{ elec/m}^2$) over the altitudes 100 to 700 km, the solar zenith angle (magenta line), and the IMF B_z in arbitrary scale. The background N_e follows a diurnal pattern with the maximum densities observed near local noon. On top of the background, N_e structures at ~ 1 hour scales near the F peak are observed both day and night. The F peak density without (with) the N_e structures is $\sim 2.0 \times 10^{11} \text{ m}^{-3}$ ($\sim 3.0 \times 10^{11} \text{ m}^{-3}$). A pattern of higher TEC or N_e structure occurrence during increased B_z magnitude is distinguishable.

[6] Figure 3a (top) shows the IMF B_z (red) and B_y (blue) components measured by the WIND spacecraft on 2009/09/15–16. The data are provided online at the NASA OmniWeb site. (Note that the online IMF data are already time-shifted (by solar wind speed) from the spacecraft to the bowshock nose. The time-shifting procedure, e.g., determination of the bowshock nose location, phase front normals, is also described at OmniWeb.) We further delayed the B_y and B_z data shown in Figure 3a by 30 min to visually match the sharp B_z southward turnings to the leading edges of the N_e enhancements. This delay is on the order of solar wind travel time along the Sun–Earth line between the bowshock nose and the RISR magnetic field line that connects to the solar wind magnetic field at the flanks of the magnetotail for B_z southward. During this period, the solar wind velocity was ~ 360 km/s. Figure 3a (middle) shows the N_e altitude profile as a function of UT with the color scale shown at the

¹Center for Geospace Studies, SRI International, Menlo Park, California, USA.

Table 1. Resolute North Radar Parameters

Parameter	Value	Units
Frequency	441.9	MHz
Peak power	1.8	MW
Duty cycle	10.0	percent
HPFB	1.0	deg.
IPP	10	ms
Range resolution	72	km
Altitude range	0–743	km
Time resolution	75	s
Magnetic dip angle	86.45–88.38	deg
Geographic latitude	74.72955 N	deg
Geographic longitude	–94.90576 E	deg
Magnetic latitude	82.77 N	deg
Magnetic longitude	323.18 E	deg
Magnetic local time	UT-7	hours
Solar local time	UT-6	hours

bottom of the plot. The black line is the total electron content in TEC units. Figure 3a (bottom) shows the anti-sunward (red line) and the dusk-to-dawn (green line) ion drift estimates from RISR. Figures 3b and 3c show the same data from days 9/20 and 9/21, except that the IMF data has been delayed by 40 and 25 min, respectively.

[7] An overview of Figure 3 is as follows: (1) The F region electron density enhancements are confined to the altitude range 250–400 km, mostly located at the F peak (300 km) and above. The peak density (including the background density) is $3 \times 10^{11} \text{ m}^{-3}$. The total TEC enhancements are up to 100%. The N_e enhancements appear to occur in response to every B_z southward turning event independent of local time. (2) The delays of the N_e enhancements are variable but still B_z events can be visually matched to N_e events, which are marked by up/down arrow heads. The duration of N_e enhancements is determined by how long B_z stays southward, e.g., on 9/15 between 2100–2400 UT. (3) We find somewhat good correlation between IMF B_z and sunward ionospheric flow in Figures 3b and 3c; however, the most predictable response of ionospheric convection is anti-sunward flow intensification to a strong B_z southward change. There exist periods showing strong correlation between B_z and sunward flow and, simultaneously, between B_y and dusk-to-dawn flow (e.g., 2009/09/15 1600–2000 UT, not shown here), correlation that is as good as shown by *Hosokawa et al.* [2006]. However, considering all the data between 9/15–9/23, and excluding the strong B_z southward turning events, the relationship between IMF and polar cap convection over Resolute is not as predictable as we expected from a simple 2-cell or 4-cell convection pattern.

[8] To further analyze the relationship between B_z - N_e and B_z -ionospheric convection, we have selected 10 events from Figure 3. The event triggers are marked by E1–E10 in Figures 3a (top), 3b (top), and 3c (top). We selected the beginning edges of density enhancements with an upward arrow for each event in Figures 3a (middle), 3b (middle), and 3c (middle). Also, we marked the ionospheric flow enhancement events with an arrow in Figures 3a (bottom), 3b (bottom), and 3c (bottom).

[9] Table 2 provides the event statistics as the following parameters from left to right: Event no, day of the month, UT (for N_e event), MLT, solar wind velocity (V_{sw}), intensity

of B_z southward turnings in nT (dB_z), duration of B_z southward turnings WB_z , duration of N_e enhancement (WN_e), the delay from B_z to N_e (N_e delay), the delay from B_z to ionospheric flow enhancement (Flow delay).

[10] Table 2 columns for WB_z and WN_e show a clear correlation between the durations of N_e enhancements and southward B_z . This data is plotted in Figure 4 (left).

[11] Figure 4 (right) shows a distribution of N_e delays in MLT. The consistent pattern of N_e enhancements around noon arriving earlier than the ones at midnight points to the cusp origin (around 75° geomagnetic latitude) of the patches. Resolute Bay can be as close as 8° (900 km) in the local noon sector to as far as 22° (2400 km) in the midnight sector to the cusp. Assuming 500 m/s anti-sunward flow speed, and a delay of ~ 10 min from the bowshock to the ionosphere [*Yu and Ridley*, 2009], the delay times would be 40 min to 90 min. These are roughly in agreement with the values in Table 2.

[12] The last column in Table 2 shows the ionospheric flow enhancement delays, which, in contrast to the N_e delays, appear to be independent of MLT (more statistics is needed to measure MLT dependence). The flow enhancements arrive (10–60 mins) earlier than the N_e enhancements. The average delay for the 10 events is 23 mins. Using the delay estimate of ~ 10 min from the bowshock to the ionosphere by *Yu and Ridley* [2009], we obtain an average delay of 13 mins, which falls in the range of mean delays between -3 and 17 mins by *Khan and Cowley* [1999] based on the EISCAT data.

[13] Figure 5 (top) shows a time-lapse (~ 75 s) sequence of the altitude profile of an individual N_e enhancement corresponding to the event 8. The enhancement peak lies between 250–300 km altitude. The N_e profile shows no clear

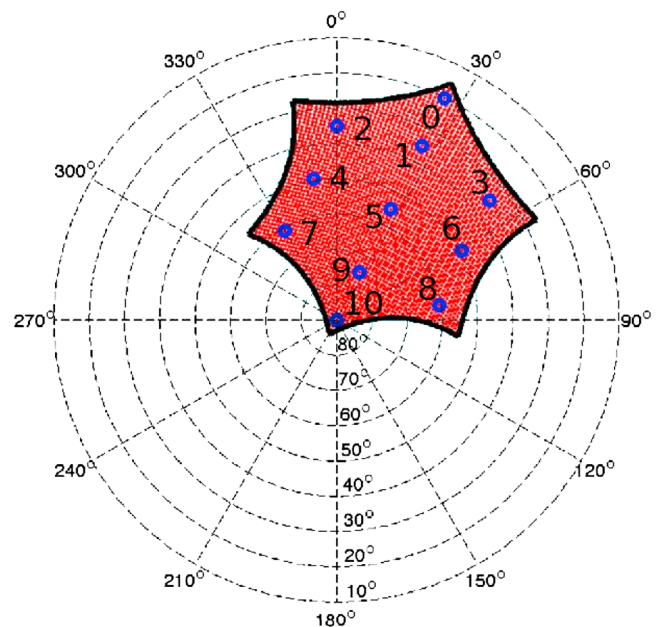


Figure 1. Azimuth and elevation boundaries of the spatial coverage of the radar. The 11 radar beam positions are marked by the circles. Geographic North (East) corresponds to 0° (90°) azimuthal directions.

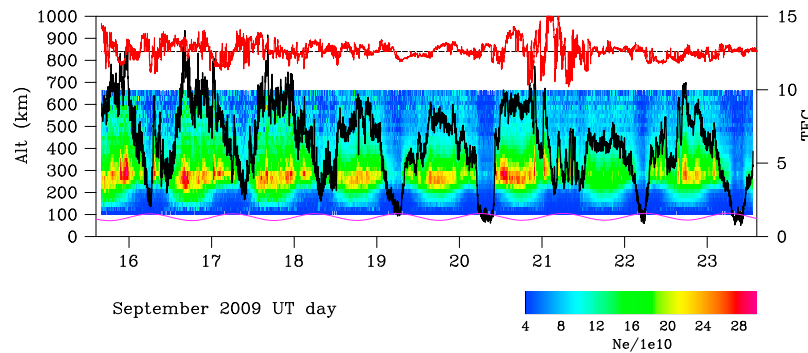


Figure 2. N_e altitude profile as a function of UT day (color plot) averaged over all look directions, the total electron content in TEC units (black line), IMF B_z (red line in arbitrary scale), and solar zenith angle (magenta line, left axis in degrees).

structure in altitude (fine altitude structure is expected in response to mono-energetic particle precipitation). Figure 5 (bottom) shows the time patterns of $N_e(300 \text{ km})$ measured by the radar beams 7, 3, and 8 (see the beam locations in Figure 5). Note the sharp and rapid rise at beam 7 at minute 209 marked by the dashed vertical line. This is followed by rapid rises at beam 8 at minute 213 and at beam 3 at minute 220. The 11 min time delay between the first peaks in B7 and B3, which are horizontally separated by $\sim 300 \text{ km}$, implies a velocity of $\sim 400 \text{ m/s}$, which is in good agreement with the mostly eastward EXB drift velocity of $\sim 400 \text{ m/s}$ observed during the event 8. The beam 3 pattern is less like the others. We think this is because the elevation of 35° is very low and, as a result, the pulse length of $480 \mu\text{s}$, which is about 70 km horizontally, smears out the sharp horizontal gradients that may be as short as 20 km . This is not the case for beams 7 and 8 because of their relatively high (60°) elevation angles.

[14] We can infer the elongation of the N_e structure perpendicular to its motion. The first $N_e(300 \text{ km})$ rise at beam 7 takes $\sim 1 \text{ min}$. For a $\sim 400 \text{ m/s}$ flow, this means a scale of 25 km . Note that beams 7 and 8 are latitudinally separated by $\sim 150 \text{ km}$. The fact that the same rise is happening at beam 8 after proper eastward EXB delay means that the structure is elongated ($>150 \text{ km}$) in the direction perpendicular to its motion, consistent with the prediction of patch formation theory by *Lockwood and Carlson* [1992].

4. Discussion and Conclusion

[15] Some of the present findings are well in line with the existing knowledge on patches [*Crowley*, 1996]. It is well-known that plasma patches are observed in the polar cap F region occurring during B_z southward. The plasma patches are thought to originate near the cusp and drift (as a result of solar wind driven ionospheric convection) in the anti-sunward direction across the polar cap. The new RISR observations contribute to previous studies made by ionosondes, radio-tomography, and airglow imagers [e.g., *MacDougall and Jayachandran*, 2007; *Walker et al.*, 1999; *Hosokawa et al.*, 2009] by simultaneously resolving the altitudinal and horizontal structuring within the N_e enhancements to $\sim 25 \text{ km}$ resolution. In summary, we find that

[16] 1. N_e enhancements are strongly tied to strong ($\geq 5 \text{ nT}$) IMF B_z southward turnings and last as long as B_z stays southward (0.5–2h in our observations). In this regard, polar patches can be regarded as tracers of strong solar wind “magnetic patches” crossing the Earth’s magnetosphere.

[17] 2. There exist substructures embedded within larger scale patches. For a select event, we observed $\sim 1 \text{ EXB}$ minutes or 20–30 km horizontal structuring in the EXB direction within an N_e enhancements that lasted 90 mins. The sharp structures were found to be elongated at least $\sim 150 \text{ km}$ in the direction of \mathbf{E} .

[18] 3. The pattern of time-delay from B_z southward turning moments to the N_e enhancements above RISR point to the cusp as their origin.

[19] 4. Altitude profiles of the leading edge of an N_e enhancement event show no clear localization in altitude that is characteristic of particle precipitation; but rather, the enhanced altitude profiles are characteristic of a solar produced plasma.

[20] 5. The most predictable feature of ionospheric convection is anti-sunward flow in response to strong B_z southward turns, compatible with the formation of the two-cell convection pattern. On average, the flow is not as simple as the two- or four-cell convection pattern.

[21] Our observations lend support to *Lockwood and Carlson’s* [1992] original hypothesis of polar cap N_e enhancements due to transient magneto-pause reconnection that occurs quasi-continuously every 1–2 minutes and that brings in solar produced plasma (as opposed to impact ionization due to cusp precipitation) across the polar cap. *Lockwood and Carlson’s* [1992] hypothesis has now been verified over the cusp in at least the European sector [*Carlson et al.*, 2004]. Furthermore, *Carlson et al.* [2006] documented the direct capture of co-rotating subauroral plasma to become injected into the polar cap; RISR observations of structures of similar nature show that their endurance over transport scales of 1000 km or more. Combining our observations with those on polar cap boundaries lends confirmation and deeper insight into the polar cap structuring processes intrinsic in transpolar plasma transport.

[22] Future studies will compare unique RISR observations of plasma density structures (provided by very rapid steering) to other radio wave (e.g., PolarDARN and Sondrestrom ISR) and optical measurements.

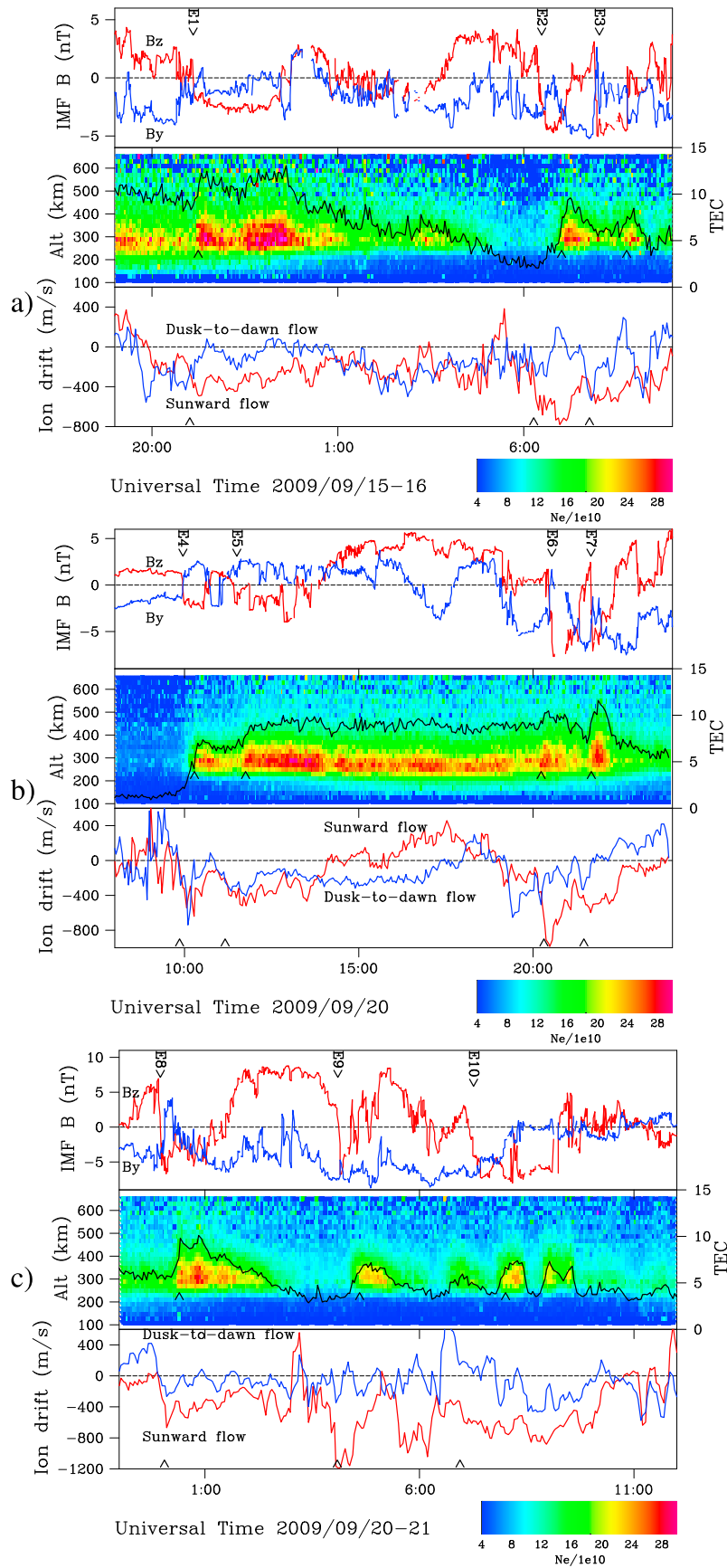
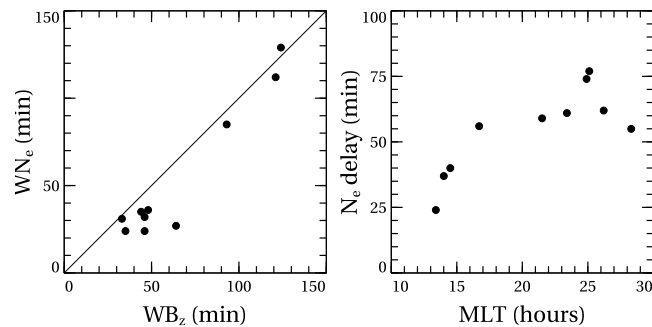


Figure 3. (a) (top) IMF B_z (red) and B_y (blue) with 30 min delay from the bowshock nose. (middle) N_e (color scale shown at the bottom) and the total electron content (dark line) in units of TEC. (bottom) Sunward (red) and dusk-to-dawn ion drift (blue). (b, c) Same as Figure 3a except that the IMF data are delayed by 40 min and 25 min from the bowshock nose, respectively.

Table 2. Statistics for Events Marked in Figure 3

Event	Day	UT	MLT	V_{sw}	dB_z	WB_z	WN_e	N_e Delay	Flow Delay
1	15	21.1	14.0	455	-3.6	124	129	37	24
2	16	6.5	23.4	463	-7.1	46	32	61	17
3	16	8.0	0.9	462	-7.9	46	24	74	15
4	20	9.9	2.2	306	-2.7	33	31	62	36
5	20	11.4	4.3	313	-1.9	121	112	55	21
6	20	20.5	13.4	345	-7.4	48	36	24	27
7	20	21.6	14.5	348	-7.4	35	24	40	30
8	20	23.8	16.7	367	-7.9	93	85	56	32
9	21	4.6	21.5	389	-5.8	44	35	59	24
10	21	8.2	1.1	389	-4.2	64	27	77	3

**Figure 4.** (left) A comparison of B_z southward and N_e enhancement durations and (right) the distribution of B_z -to- N_e delays in MLT.

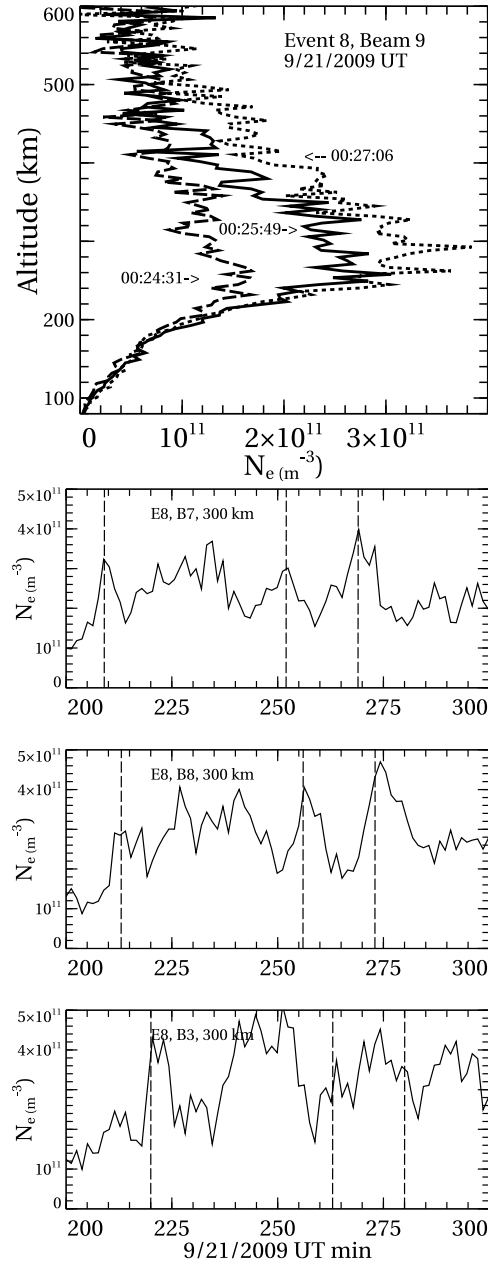


Figure 5. (top) Change of the altitude profile of N_e for Event 8 at 75 s increments from left to right, dashed, solid and dotted lines, respectively. (bottom) The passage of a train of small scale N_e enhancements through beams 7, 8, and 3 (see Figure 1), observed at 300 km altitude. The first vertical lines mark the minutes 209, 213, and 220, from top to bottom. The time shifts of the following two vertical lines relative to the first are the same for all the beams.

[23] **Acknowledgments.** RISR was developed under the NSF cooperative agreement ATM-0121483 to SRI International and the operations and maintenance is supported by NSF cooperative agreement ATM-0608577 to SRI International.

References

- Carlson, H. C., Jr., K. Oksavik, J. Moen, and T. Pedersen (2004), Ionospheric patch formation: Direct measurements of the origin of a polar cap patch, *Geophys. Res. Lett.*, *31*, L08806, doi:10.1029/2003GL018166.
- Carlson, H. C., J. Moen, K. Oksavik, C. P. Nielsen, I. W. McCreca, T. R. Pedersen, and P. Gallop (2006), Direct observations of injection events of subauroral plasma into the polar cap, *Geophys. Res. Lett.*, *33*, L05103, doi:10.1029/2005GL025230.
- Crowley, G. (1996), Critical review of ionospheric patches and blobs, in *Review of Radio Science 1993–1996*, edited by W. R. Stone, pp. 619–648, Oxford Univ. Press, New York.
- Hosokawa, K., K. Shiokawa, Y. Otsuka, A. Nakajima, T. Ogawa, and J. D. Kelly (2006), Estimating drift velocity of polar cap patches with all-sky airglow imager at Resolute Bay, Canada, *Geophys. Res. Lett.*, *33*, L15111, doi:10.1029/2006GL026916.
- Hosokawa, K., T. Kashimoto, S. Suzuki, K. Shiokawa, Y. Otsuka, and T. Ogawa (2009), Motion of polar cap patches: A statistical study with all-sky airglow imager at Resolute Bay, Canada, *J. Geophys. Res.*, *114*, A04318, doi:10.1029/2008JA014020.
- Khan, H., and S. W. H. Cowley (1999), Observations of the response time of high-latitude ionospheric convection to variations in the interplanetary magnetic field using EISCAT and IMP-8 data, *Ann. Geophys.*, *17*, 1135–1306.
- Lockwood, M., and H. C. Carlson Jr. (1992), Production of polar cap electron density patches by transient magnetopause reconnection, *Geophys. Res. Lett.*, *19*, 1731–1734.
- MacDougall, J., and P. T. Jayachandran (2007), Polar patches: Auroral zone precipitation effects, *J. Geophys. Res.*, *112*, A05312, doi:10.1029/2006JA011930.
- Walker, I. K., J. Moen, L. Kersley, and D. A. Lorentzen (1999), On the possible role of cusp/cleft precipitation in the formation of polar-cap patches, *Ann. Geophys.*, *17*, 1298–1305.
- Yu, Y., and A. J. Ridley (2009), Response of the magnetosphere-ionosphere system to a sudden southward turning of interplanetary magnetic field, *J. Geophys. Res.*, *114*, A03216, doi:10.1029/2008JA013292.

H. Bahcivan, C. Heinselman, M. Nicolls, and R. Tsunoda, Center for Geospace Studies, SRI International, 333 Ravenswood Ave., Menlo Park, CA 94025, USA. (hasan.bahcivan@sri.com)